Supporting Information

In-situ Infrared Spectroscopy Reveals Persistent Alkalinity Near Electrode Surfaces during CO_2 Electroreduction

Kailun Yang†, Recep Kas†, Wilson A. Smith*

*correspondence should be addressed to: w.smith@tudelft.nl

† These authors contributed equally to the manuscript.

Index **Page**

Mass transport simulations

The concentrations of the (electro)active molecules within the diffusion layer were modelled as a 1-D system which took into account diffusion and bubble induced mass transfer.[1-3] Bubble induced mass transfer was included to the model by approximating the change in the diffusion layer thickness as a function of the current density.[1] Evolution of gas bubbles from the electrode surface is considered to contribute to the mass transport of reactants and products during their growth, break-off and induced wake flow. These effects are thoroughly described by Vogt et al.[4] and recently applied to describe nanomorphology induced mass transport during CO_2 electroreduction.[1] Rousar correlation[5] was used to include the convectional effect created during the departure of the bubbles (Sh1) while the Vogt. relation[4] was used to describe the convectional effect of bubble growth and wake flow (Sh2).

$$Sh1 = \sqrt{\frac{12}{\pi}}\, Re_g^{0.5}\, Sc^{0.34}\, \Theta^{0.5}$$

$$Sh2 = \sqrt{\frac{12}{\pi}}\, Re_g^{0.5}\, Sc^{0.34}\, (1 - \frac{\sqrt{8}}{3}\, \frac{R_a}{R}\, \Theta)(1 + \Theta)$$

where Θ is the fraction of the electrode area covered by the bubbles and R_a/R is the ratio of the contact length of a single bubble to its diameter. The Reynolds number (Re_g) and Schmidt number (Sc) for gas evolution are given by the following:

$$Re_g = \frac{V_{gas}}{A}\frac{d_b}{\nu}$$

$$\mathrm{Sc} = \frac{\nu}{D}$$

where d_b is the average departure diameter of the bubbles and ν is the kinematic viscosity. The departure diameter of the bubbles are commonly assumed to be 50 μm for electrodes with horizontal planes facing upward.[6] Departure diameter of the bubbles (d_b) was measured with imaging lenses (Edmund optics) to justify this assumption for different electrolyte concentrations (Figure S20). The coverage of the bubbles were taken as 0.05 based on the hydrogen evolution data on metal electrodes[7] and R_a/R is assumed to be 0.75.[4]

The Reynolds number and current density can be correlated by calculating the area normalized volume flux due to gas evolution by;

$$\frac{V_{gas}}{A} = \frac{J}{nF}\frac{RT}{P}$$

where P is pressure, T is temperature, R is the gas constant, n is average number of electrons transferred for gaseous products, F is the Faraday constant, J is the current density for gaseous products.

The mass transport number for bubble induced convection can be derived from the Sheerwood number (Sh_{bubble}) which can be obtained by combining Sh1 and Sh2 in the following equations:

$$Sh_{bubble} = (\, Sh_1^2 + \, Sh_2^2 \,)^{0.5}$$

$$k_{bubble} = \frac{Sh_{bubble}\, D_i}{d_b}$$

where D_i is the diffusivity of the molecule of interest and k_{bubble} is the mass transport number for bubble induced convection. This number can be correlated to the double layer thickness(σ) via the equation;

$$\sigma = \frac{D_i}{k_{bubble}}$$

The change in the double layer thickness as a function of current density is given in Figure S21.

By considering the change in the double layer thickness as a function of current density, the concentration of molecules within the boundary layer was calculated by using the Nernst-Planck equation.[1-3, 8] Due to high electrolyte concentration, the effect of migration on the transport of the molecules from the bulk to the surface was assumed to be negligible. In addition, the concentration of molecules in the bulk was considered to be at their equilibrium concentrations for reactions 1 to 6 given below. CO_2 and/or water molecules are consumed at the cathode to produce CO_2 reduction products and hydrogen, while the produced OH^- is neutralized by the following equilibria and reactions.[4]

$H_3PO_{4(aq)} + OH^-_{(aq)}$ <--> $H_2PO_4^-{}_{(aq)} + H_2O$ (1)

$H_2PO_4^-{}_{(aq)} + OH^-_{(aq)}$ <--> $HPO_4^{2-}{}_{(aq)} + H_2O$ (2)

$\mathbf{HPO_4^{2-}_{(aq)} + OH^-_{(aq)} <--> PO_4^{3-}_{(aq)} + H_2O}$ **(3)**

$\mathbf{CO_{2(aq)} + OH^-_{(aq)} <-> HCO_3^-_{(aq)}}$ **(4)**

$\mathbf{HCO_3^-_{(aq)} + OH^-_{(aq)} <-> CO_3^{2-}_{(aq)} + H_2O}$ **(5)**

The equilibrium constant for these reactions are K_1= 6.92×10^{11} M^{-1}, K_3= 4.79×10^{1} M^{-1}, K_4= 4.44×10^{7} M^{-1} and K_5= 4.66×10^{3} M^{-1}.[2-3] For the reaction 2, which is the parent buffer reaction, apparent K_2 values are calculated based on activity coefficients[9] and used to estimate the initial pH of the solutions before CO_2 purging with the following approach.

$$K_2 = \frac{a_{HPO_4^{2-}}}{a_{OH^-}\ a_{H_2PO_4^-}} = \frac{\gamma_{HPO_4^{2-}}[HPO_4^{2-}]}{\gamma_{OH^-}[OH^-]\ \gamma_{H_2PO_4^-}[H_2PO_4^-]} = \text{apparent } K_2 = \frac{[HPO_4^{2-}]}{[OH^-]\ [H_2PO_4^-]}$$

When the parent phosphate solution is purged with the CO_2 the following reaction takes places to form bicarbonate.

$\mathbf{H_2PO_4^-_{(aq)} + CO_{2(aq)} + H_2O <-> H_2PO_4^-_{(aq)} + HCO_3^-_{(aq)}}$ **(6)**

The equilibrium concentrations of the respective ions for reaction 6 can be calculated by using the reactions 2 and 4 and equilibrium constants K_2 and K_4.

The forward rate constants for phosphate buffer reactions (1-3) were assumed to be on the order of fast acid-base reactions and taken as 1×10^{10} $M^{-1}s^{-1}$,[10] while the forward reaction rate for reaction (4) is 5.93×10^{3} $M^{-1}s^{-1}$.[2] The forward reaction rate of reaction (5) is assumed to be 1×10^{8} $M^{-1}s^{-1}$.[2] The corresponding backward reaction rates were calculated from equilibrium constants. Diffusion coefficients were corrected for viscosity by using Stokes-Einstein equation. [11]

The concentration of the molecules within the diffusion layer and at the surface can be extracted by solving the following coupled differential equations:

$$\frac{\delta[H_3PO_4]}{\delta x} = D_{H_3PO_4}\frac{\delta^2[H_3PO_4]}{\delta x^2} - k_{1f}[H_3PO_4]*[OH^-] + k_{1b}[H_2PO_4^-]$$

$$\frac{\delta[H_2PO_4^-]}{\delta x} = D_{H_2PO_4^-}\frac{\delta^2[H_2PO_4^-]}{\delta x^2} + k_{1f}[H_3PO_4]*[OH^-] - k_{1b}[H_2PO_4^-] - k_{2f}[H_2PO_4^-][OH^-] + k_{2b}[HPO_4^{2-}]$$

$$\frac{\delta[HPO_4^{2-}]}{\delta x} = D_{HPO_4^{2-}}\frac{\delta^2[HPO_4^{2-}]}{\delta x^2} + k_{2f}[H_2PO_4^-][OH^-] - k_{2b}[HPO_4^{2-}] - k_{3f}[HPO_4^{2-}][OH^-] + k_{3b}[PO_4^{3-}]$$

$$\frac{\delta[PO_4^{3-}]}{\delta x} = D_{PO_4^{3-}}\frac{\delta^2[PO_4^{3-}]}{\delta x^2} + k_{3f}[HPO_4^{2-}][OH^-] - k_{3b}[PO_4^{3-}]$$

$\frac{\delta[CO_2]}{\delta x} = D_{CO_2} \frac{\delta^2[CO_2]}{\delta x^2}$-$k_{4f}[CO_2][OH^-]$+$k_{4b}[HCO_3^-]$

$\frac{\delta[HCO_3^-]}{\delta t} = D_{HCO_3^-} \frac{\delta^2[HCO_3^-]}{\delta x^2}$+ $k_{4f}[CO_2][OH^-]$-$k_{4b}[HCO_3^-]$-$k_{5f}[HCO_3^-][OH^-]$+ $k_{5b}[CO_3^{2-}]$

$\frac{\delta[CO_3^{2-}]}{\delta t} = D_{CO_3^{2-}} \frac{\delta^2[CO_3^{2-}]}{\delta x^2}$+ $k_{5f}[HCO_3^-][OH^-]$- $k_{5b}[CO_3^{2-}]$

$\frac{\delta[OH^-]}{\delta t} = D_{OH^-} \frac{\delta^2[OH^-]}{\delta x^2}$-$k_{4f}[CO_2][OH^-]$+$k_{4b}[HCO_3^-]$ $-k_{1f}[H_3PO_4]$*$[OH^-]$+$k_{1b}[H_2PO_4^-]$ $k_{2f}[H_2PO_4^-][OH^-]$+k_{2b} $[HPO_4^{2-}]$- $k_{3f}[HPO_4^{2-}][OH^-]$+k_{3b} $[PO_4^{3-}]$ -$k_{5f}[HCO_3^-][OH^-]$+ $k_{5b}[CO_3^{2-}]$

Sixteen boundary conditions were given in the Table SI1 to solve eight second order time dependent partial differential equations for concentration of the species of H_3PO_4, $H_2PO_4^-$,HPO_4^{2-} ,PO_4^{3-}, CO_2, OH^-, HCO_3^- and CO_3^{2-} at the surface and boundary layer. Bulk solution is where the distance from the electrode surface is larger than the boundary layer thickness. It is assumed to have infinite supply of molecules from the bulk.

The first boundary condition is based on the flux of the reactants and products which can be related to the partial current density of the reactants and products for an electrochemical reaction.

$$D_{CO_2} \frac{\delta[CO_2]}{\delta x} = CO_{2\ consumption}$$

$$D_{OH^-} \frac{\delta[OH^-]}{\delta x} = OH^-_{production}$$

CO_2 consumption and OH^- production can be related to current density by the following equations.

$CO_{2\ consumption} = \frac{J}{F}(\sum_i a_i \frac{x_i}{n_i})$

$OH^-_{\ production} = \frac{J}{F}(\sum_i x_i)$

Where a_i is the number of moles CO_2 molecules consumed per moles of product. x_i is the current efficiency and n_i is the number of electrons transferred for the following reactions. These values are given in Table SI 3. (pls note that the deprotonation of formic acid to formate must to be excluded).

CO_2 + H_2O + $2e^-$ <-> $HCOO^-$ + OH^-

$CO_{2(aq)}$ + H_2O + $2e^-$ <-> CO + $2OH^-$

$2CO_{2(aq)}$ + $8H_2O$ + $12e^-$ <-> C_2H_4+ $12OH^-$

$CO_{2(aq)} + 6H_2O + 8e^- <-> CH_4 + 8OH^-$

$2H_2O + 2e^- <-> H_2 + 2OH^-$

The second boundary condition is that at the solution edge of the boundary layer the concentration of the molecules are equal to the equilibrium concentrations (i.e. bulk) when a constant current is applied (t>0). The initial values of the concentrations, before a galvanostatic step is applied, are assumed to be the same as the bulk concentrations (t=0)

and are listed in Table 4 for different electrolyte

concentrations.

To account for solubility of CO_2 in different electrolyte concentrations, the following Sechenov Equation was used;[12]

$$\text{Log}\left(\frac{CO_2^{water}}{CO_2^{electrolyte}}\right) = \sum(h_G + h_{ion})\, C_i$$

where h_G can be approximated by and all parameters are given Table 2;

$$h_G = h_{G,0} + h_T(T - 298.15)$$

All the parameters are given in Table SI2.

Formation of oxygenates on nanowires: Drawing structure-activity relationships requires very careful designed set of experiments on well-defined surfaces, e.g single crystals, shape controlled nanoparticles, by using in-situ and/or online techniques addressing structural changes on catalyst surface and reaction intermediates. Poorly defined surfaces, such as randomly grown nanowires, are very vulnerable to not only mass transport effects but also structural changes during the electroreduction experiments which are not straightforward to identify. Therefore, we don't find it convenient to draw structure activity relationships purely based on catalytic activity and selectivity studies on ill-defined surfaces. The FE and partial current density of ethanol, acetate and propanol are given for nanowire electrodes as a function of electrolyte concentration in Figure S8 and Figure S10, respectively. Acetaldehyde is considered to be intermediate for ethanol and acetate formation during CO_2 electroreduction.[13-14] Both electrochemical and non-electrochemical pathways were proposed. Non-electrochemical pathway was suggested to take place via disproportionation of aldehydes by high local pH (or bulk pH for CO reduction).[15] Therefore, local alkaline conditions as a result of poor mass transport might favour the formation of these two product. This partially explains formation of ethanol and acetate on copper surfaces. However, the higher production rates of ethanol compared to acetate, in agreement with literature for different copper surfaces, implies existence of another pathway for the formation of ethanol. Single crystal studies suggested that this pathway is structure sensitive and ethylene vs ethanol selectivity should be able to tuned by catalyst structure.[14] We think dissolution, re-deposition and surface reconstruction under OCP and/or cathodic potentials challenges both fundamental and

practical studies. Propanol is one of the least studied compounds among the detected products. Different pathways proposed.[16] First of all, interestingly, no propionic acid is detected to the best of our knowledge in most of the studies. This partially rules out the effect of Cannizaro type of reactions on the mechanism. We believe propanol is formed via insertion of CO to an C2 intermediate which is improved most likely by re-adsorption effects in porous structures. Production of propanol therefore most likely be influenced by formation C2 compounds, CO formation and/or coverage. Recently, mesoscale and morphological effects was identified as key parameter for the enhanced formation of propanol.[17] However, smooth copper electrodes are also capable of making minor amount of propanol.[18]

C2 products were considered to be formed via an early CO coupling.[19] Propanol is the only C3 product observed in appreciable amount and the pathway towards propanol is not clear yet. Considering the fact that propanol is nearly always accompany the C2 products, we think it is formed by a CO insertion to an C_2 intermediate. Therefore C2 and C3 products are considered to be formed via common rate determining step while the individual selectivity's are determined by the catalyst structure[20], kinetic barriers,[21] mesoscale effects,[22] and possibly CO coverage.[23] We think the total production rate of these products are important rather than only ethylene and the summation of partial current density for C2 and C3 products is very similar for different electrolyte concentrations. The increase in the formation of methane at high electrolyte concentration takes places "mostly" at the expense of ethanol and propanol rather than ethylene (Figure 3 main text and FigureSI 10). Pls note that at low electrolyte concentration(0.1M) mass transfer limited current density is slightly lower which also partially explains the lower production of ethylene.

t>0 at the electrode surface	t>0 in the bulk solution
$D_{H_3PO_4}\frac{\delta[H_3PO_4]}{\delta x^2}=0$	$H_3PO_4 = [H_3PO_4]_i$
$D_{H_2PO_4^-}\frac{\delta[H_2PO_4^-]}{\delta x^2}=0$	$H_2PO_4^- = [H_2PO_4^-]_i$
$D_{HPO_4^{2-}}\frac{\delta[HPO_4^{2-}]}{\delta x^2}=0$	$HPO_4^{2-} = [HPO_4^{2-}]_i$
$D_{PO_4^{3-}}\frac{\delta[PO_4^{3-}]}{\delta x}=0$	$PO_4^{3-} = [PO_4^{3-}]_i$
$D_{CO_2}\frac{\delta[CO_2]}{\delta x}=CO_{2\ consumption}$	$CO_2 = [CO_2]_i$
$D_{OH^-}\frac{\delta[OH^-]}{\delta x}=OH^-_{production}$	$OH^- = [OH^-]_i$
$D_{HCO_3^-}\frac{\delta[HCO_3^-]}{\delta x^2}=0$	$HCO_3^- = [HCO_3^-]_i$
$D_{CO_3^{2-}}\frac{\delta[CO_3^{2-}]}{\delta x^2}=0$	$CO_3^{2-} = [CO_3^{2-}]_i$

Table SI 1: Boundary conditions to solve time dependent differential equations.

Parameter	value
$\mathbf{D_{H_3PO_4}}$	8.7x10^{-10} m^2 s^{-1}
$\mathbf{D_{H_2PO_4^-}}$	8.46x10^{-10} m^2 s^{-1}
$\mathbf{D_{HPO_4^{2-}]}}$	6.9x10^{-10} m^2 s^{-1}
$\mathbf{D_{PO_4^{3-}}}$	6.12*10^-10 m^2 s^{-1}
$\mathbf{D_{OH^-}}$	5.27x10^{-9} m^2 s^{-1}
$\mathbf{D_{CO_2}}$	1.91x10^{-9} m^2 s^{-1}
$\mathbf{CO_2}$ $\boldsymbol{h_{G,0}}$	-0.0172 m^3 kmol^{-1}
$\mathbf{CO_2}$ $\boldsymbol{h_T}$	-0.000338 m^3 kmol^{-1}
$\mathbf{H_2PO_4^-}$ $\boldsymbol{h_{ion}}$	0.1009 m^3 kmol^{-1}
$\mathbf{HPO_4^{2-}}$ $\boldsymbol{h_{ion}}$	0.1559 m^3 kmol^{-1}
$\mathbf{K^+}$ $\boldsymbol{h_{ion}}$	0.0929 m^3 kmol^{-1}

Table SI 2: Simulation parameters. Pls not that diffusion coefficients were corrected for each electrolyte concentration by using Stokes-Einstein relation.

	H_2	CO	C_2H_4	CH_4	Formate
x_i	**0.5**	**0.01**	**0.1**	**0.25**	**0.1**
n_i	**2**	**2**	**12**	**8**	**2**
a_i	**0**	**1**	**2**	**1**	**1**

Table SI 3: a_i is the number of moles CO_2 molecules consumed per moles of product. x_i is the current efficiency and n_i is the number of electrons transferred for the following reactions.

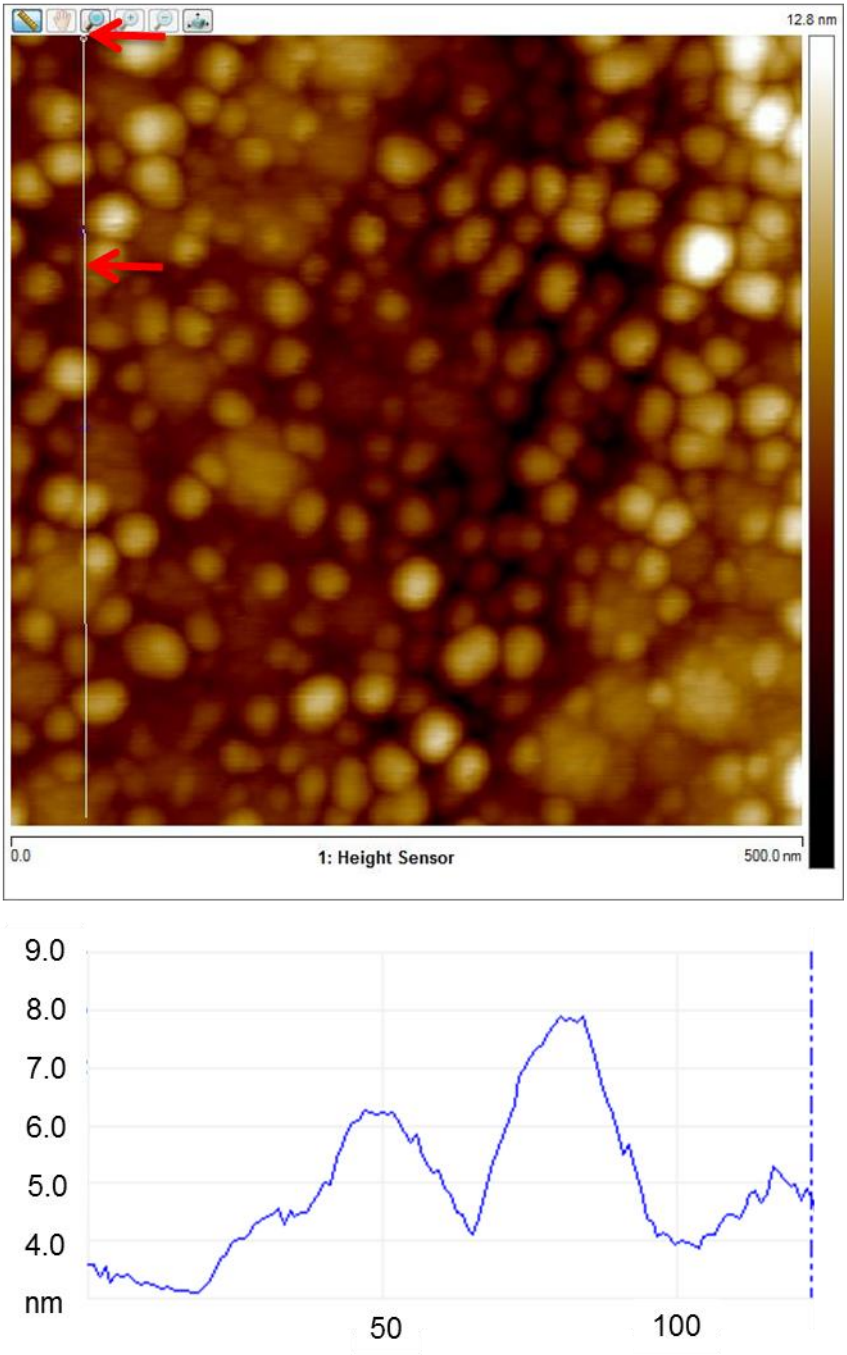

Figure S1: AFM image and height profile of Cu film on Ge along (red) marked direction

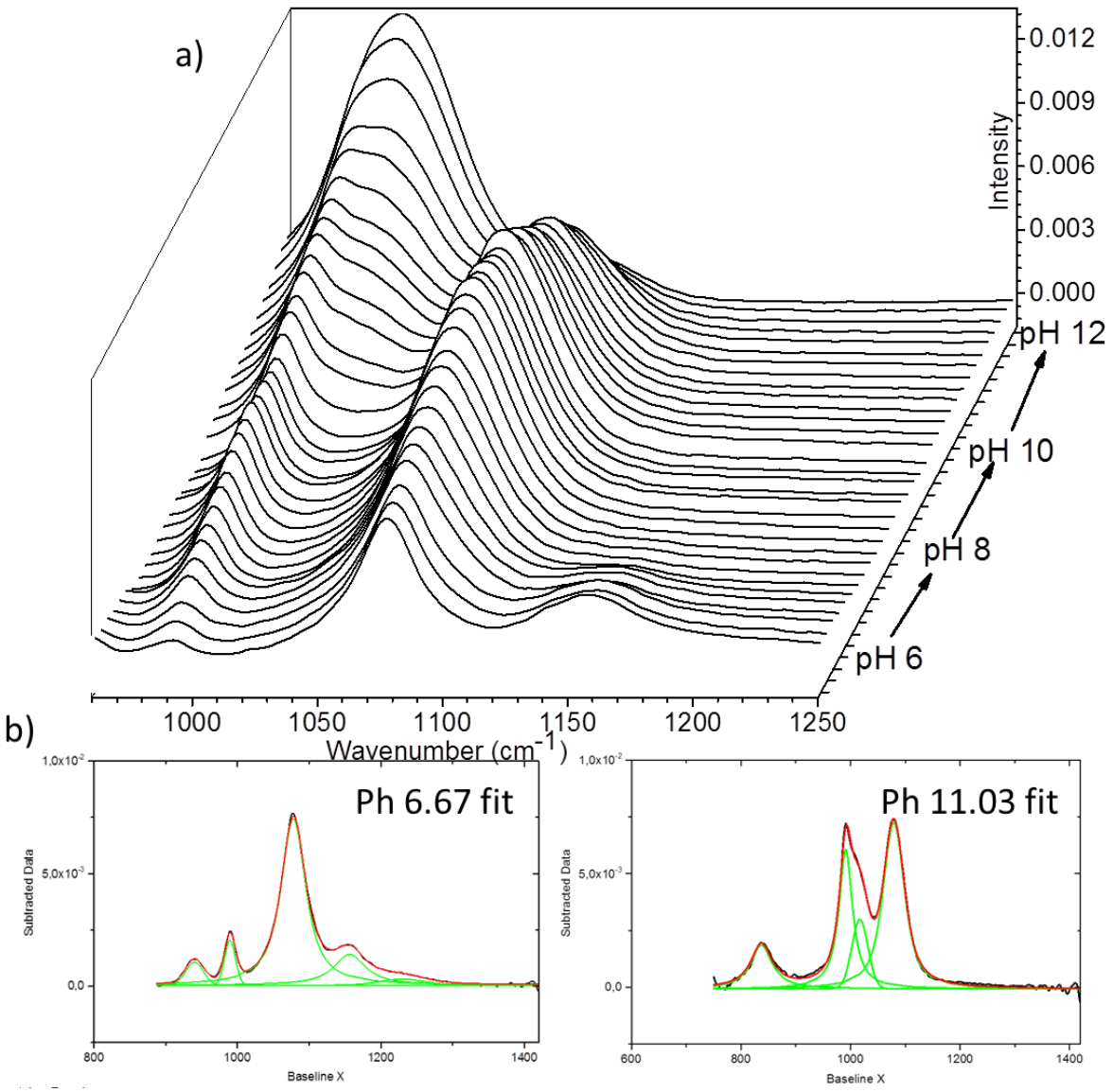

Figure S2: a) SEIRA spectra of phosphate species for different pH values between 6 and 12 under an applied potential of +0.1 V vs RHE. The spectra were obtained by addition of KOH to parent KH_2PO_4 solution. **b)** Individual peaks for each phosphate species were deconvoluted by using OriginPro

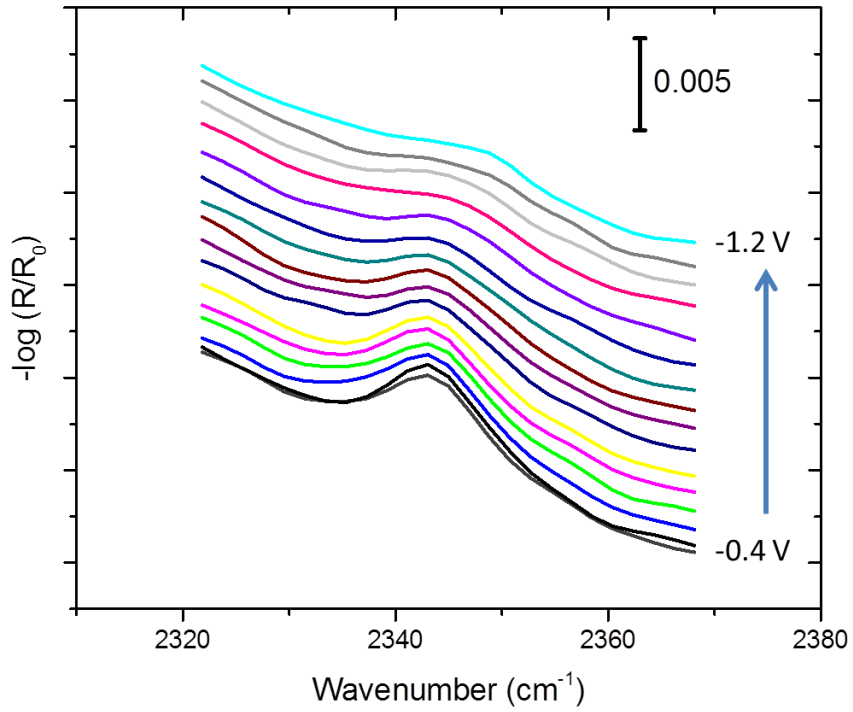

Figure S3: Potential dependent changes in the asymmetrical stretching of CO_2(aq)

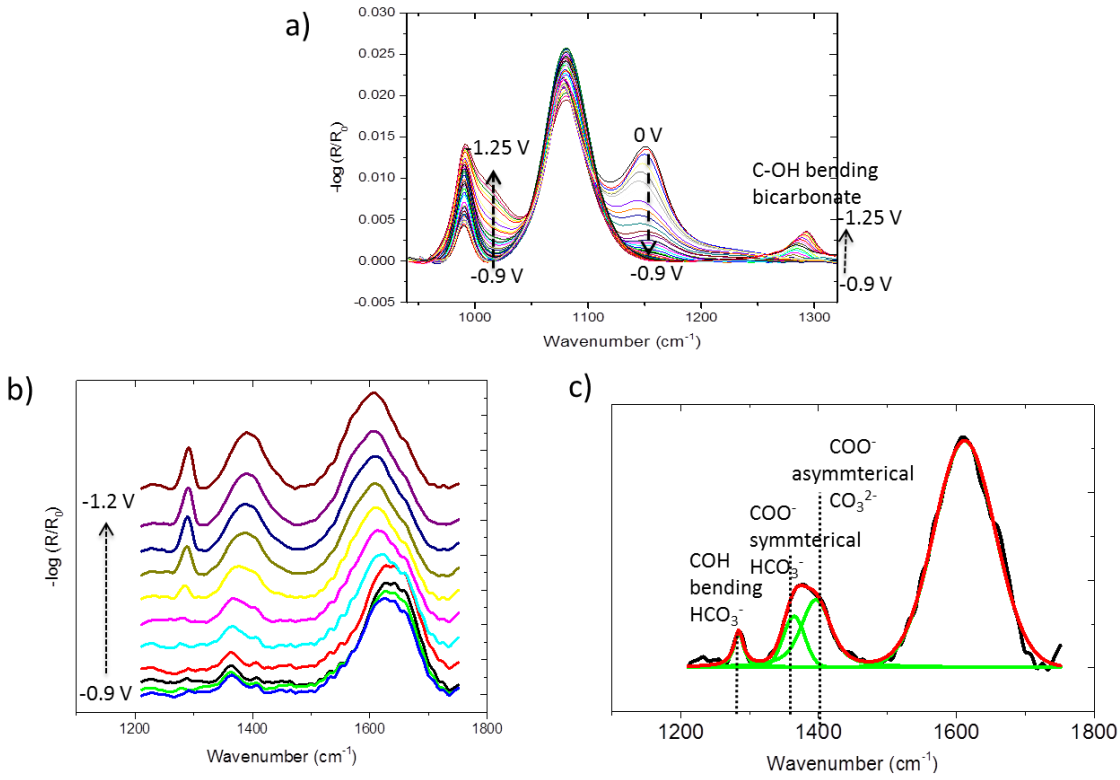

Figure S4: a) Detection of bicarbonate coincides with alkaline pH (>9) near the electrode surface. b) Change in (bi)carbonate and water bands at high potential region c) Individual peaks for (bi)carbonate species were deconvoluted by using OriginPro. Pls note that bicarbonate has another mode overlapping with water and usually hard to deconvolute.

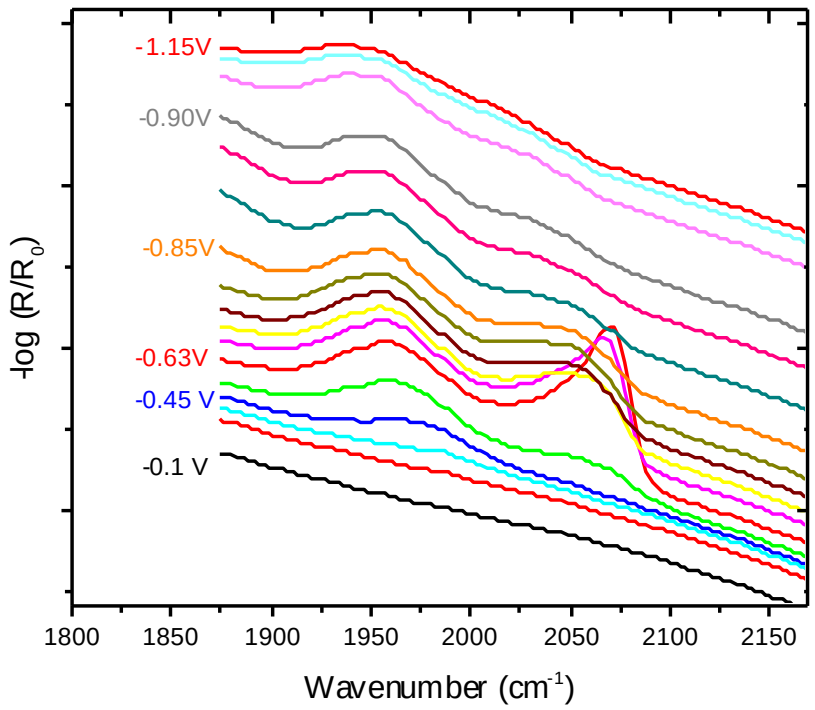

Figure S5: Adsorption of CO as a function of potential given for 0.5 M phosphate buffer.

i

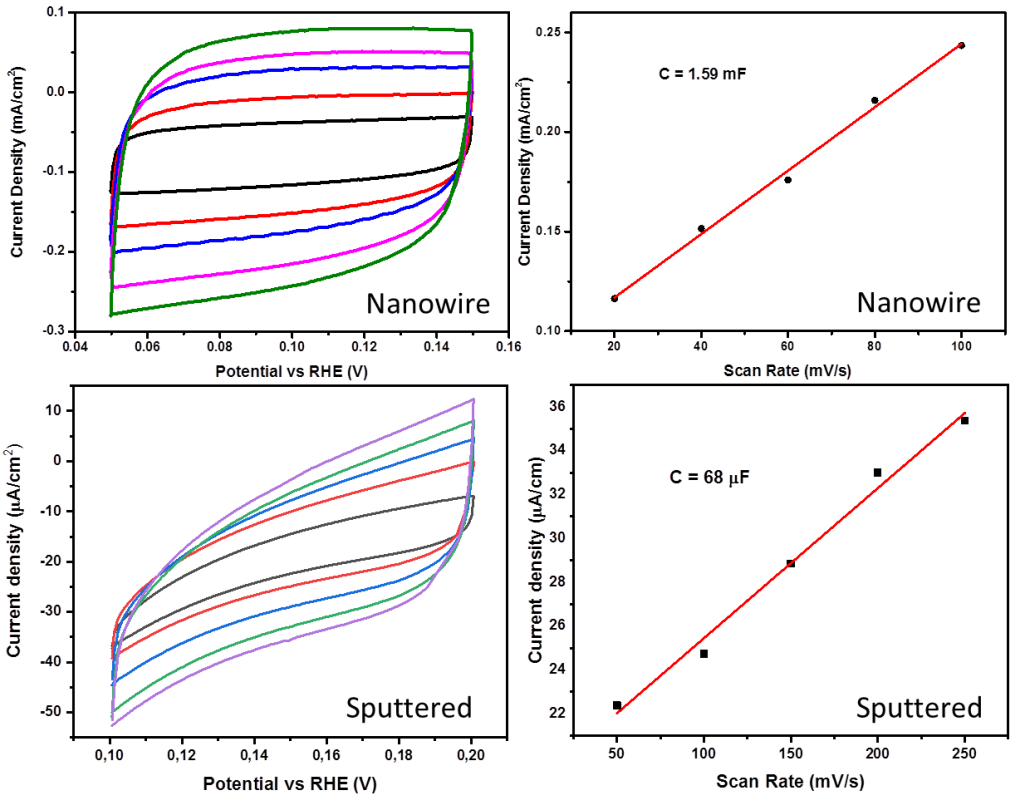

Figure S6 Determination of double layer capacitance and roughness factor in 0.1 M $NaClO_4$ for Nanowire and sputtered copper electrodes.

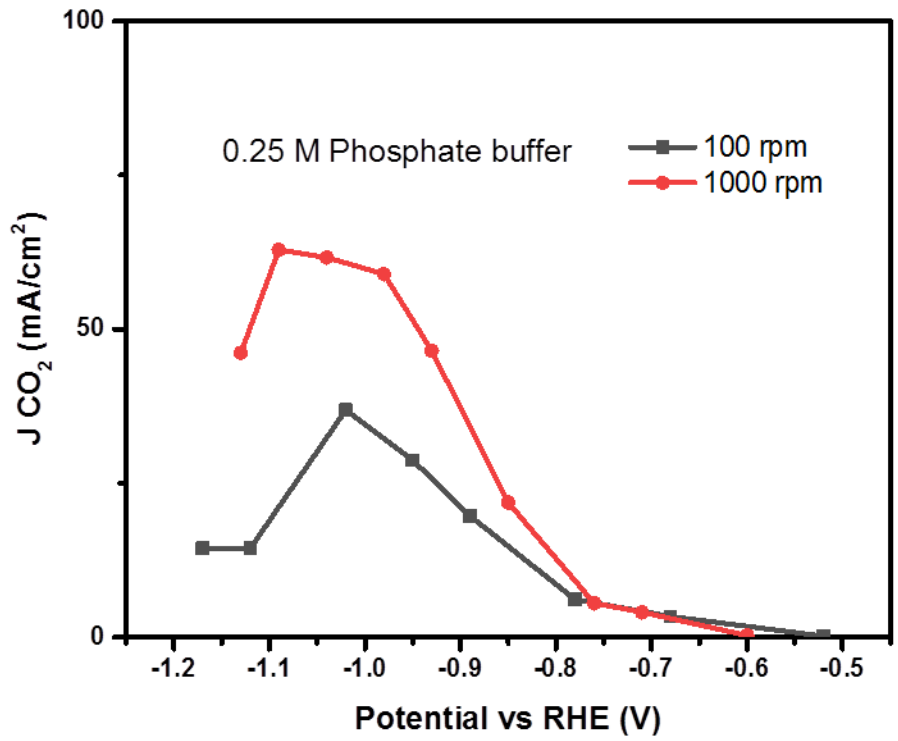

Figure S7: Effect of stirring on the partial current density of CO_2 reduction.

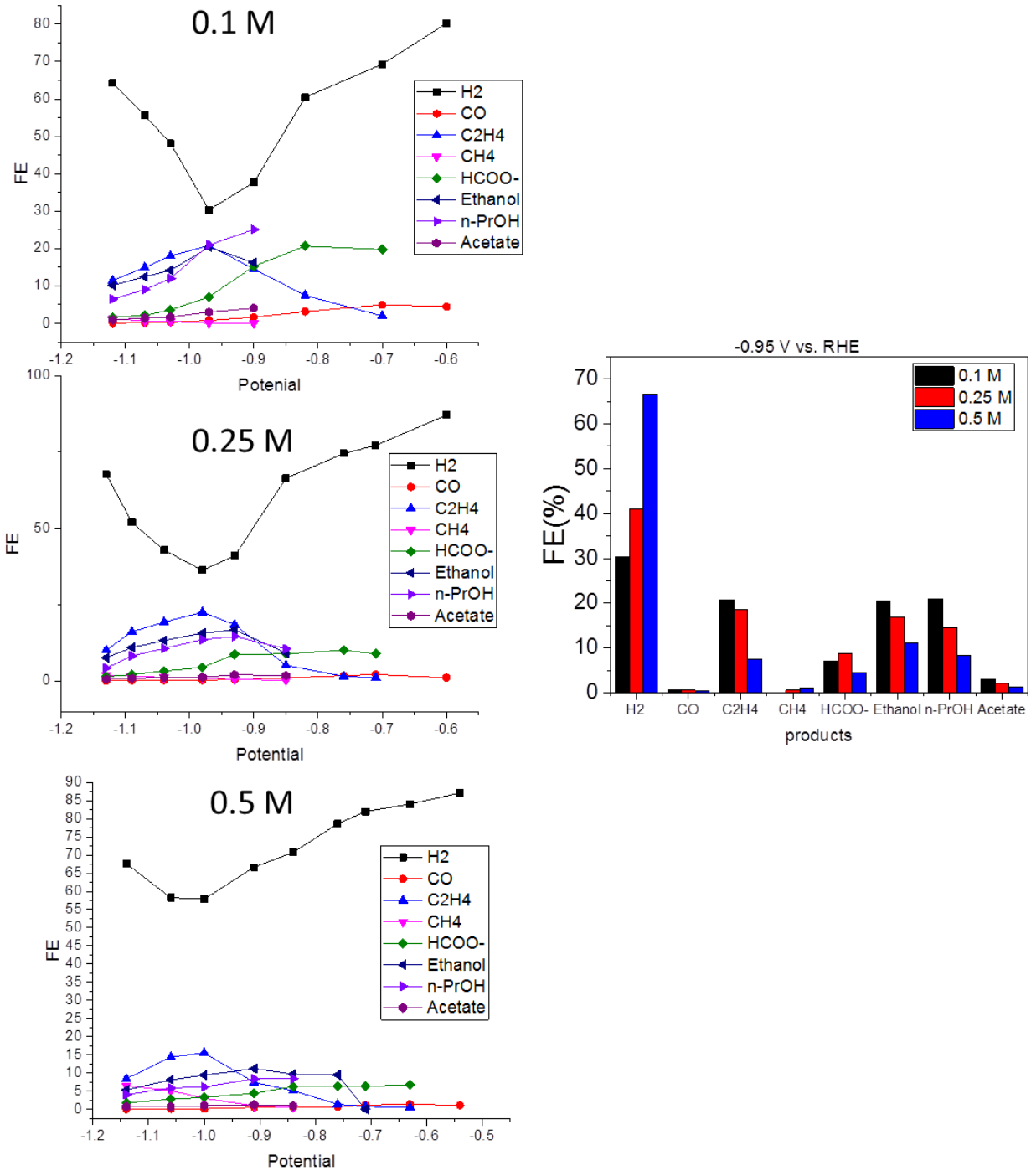

Figure S8: Faradaic efficiency of gaseous and liquid products as a function of electrolyte concentration for nanowire copper electrodes.. The electrolytes are composed of equimolar amounts of $H_2PO_4^-$ and HPO_4^{2-}. FE of hydrogen increased notably at higher electrolyte concentrations and the selectivity towards C_2 and C_3 products decreased at potentials between -0.7 V vs RHE to -1 V vs RHE as a function of electrolyte concentration. The decrease in the selectivity of CO_2 reduction products are mostly result of increase in the hydrogen production (see main text).

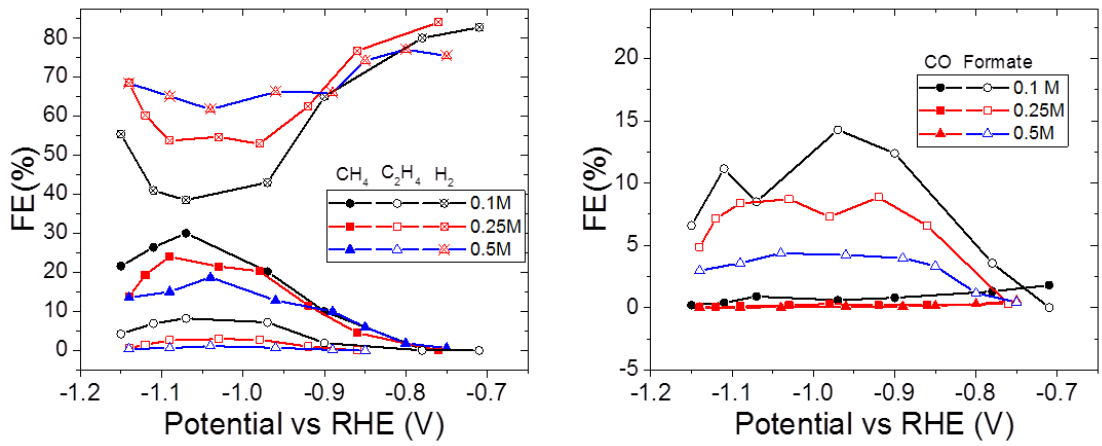

Figure S9: Faradaic efficiency of gaseous and liquid products as a function of electrolyte concentration for sputtered copper electrodes.. The electrolytes are composed of equimolar amounts of $H_2PO_4^-$ and HPO_4^{2-}. FE of hydrogen increased notably at higher electrolyte concentrations and the selectivity towards C_1 and C_2 products decreased at potentials between -0.8 V vs RHE to -1.1 V vs RHE as a function of electrolyte concentration. The decrease in the selectivity of CO_2 reduction products are mostly result of increase in the hydrogen production (see main text).

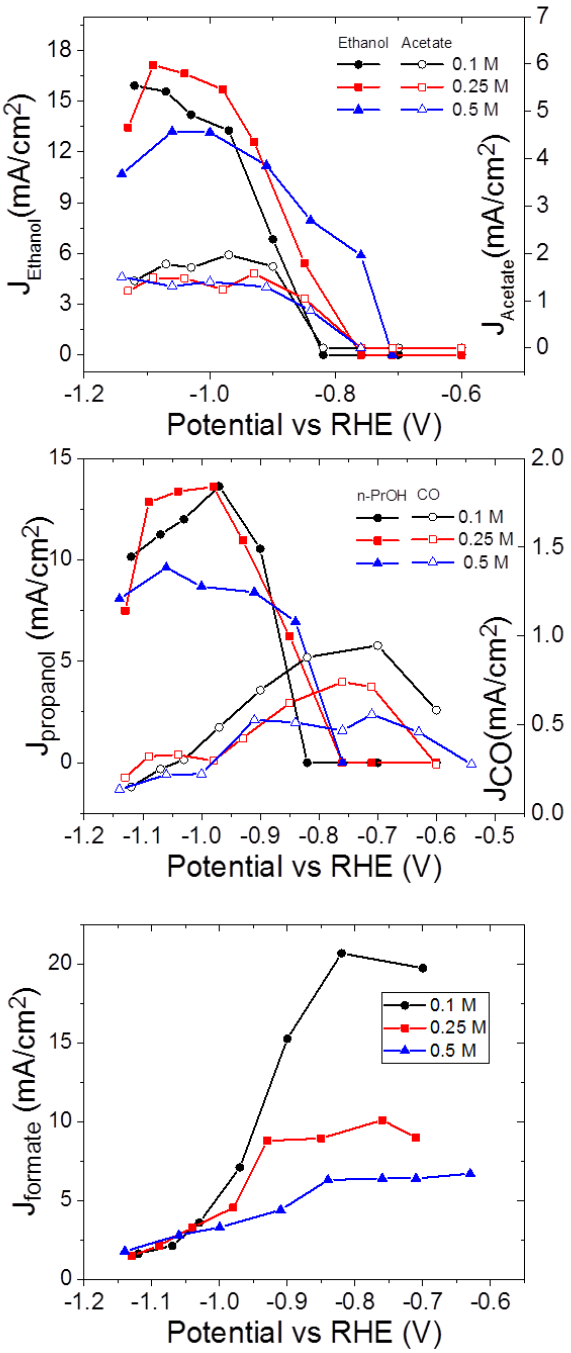

Figure S10: Partial current density of of gaseous and liquid products as a function of electrolyte concentration for nanowire electrodes. Partial current density of Methane, Ethylene and Hydrogen are given in main text.

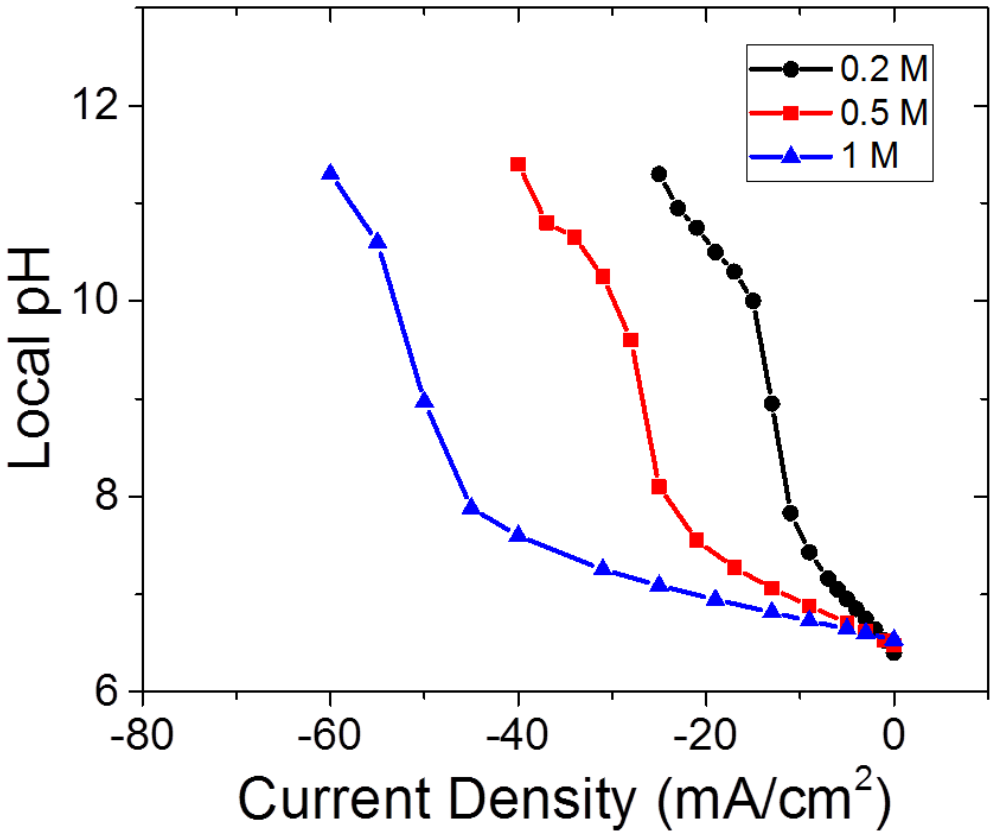

Figure S11: Local pH as a function of current density calculated by including diffusion and convection via stirring (without bubble induced convection). Double layer thickness is taken as 100 µm which is a typical thickness that can be achieved with extensive magnetic stirring. This value is used commonly for calculating near surface concentration of molecules during CO_2 electroreduction.[2-3] This graph indicates the model dramatically underestimates the buffer capacity without bubble induced mass transport term at high currents (> 20 mA/cm^2).

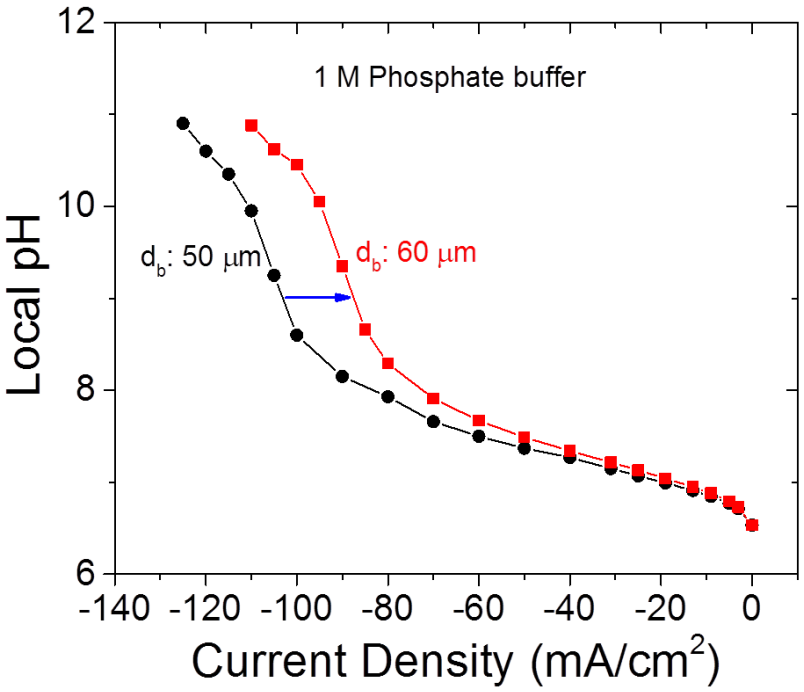

Figure S12: Local pH as a function of current density calculated by bubble induced mass transport model for two different bubble departure diameters (d_b). The difference after breakdown of the buffer is notably high compared to buffered region.

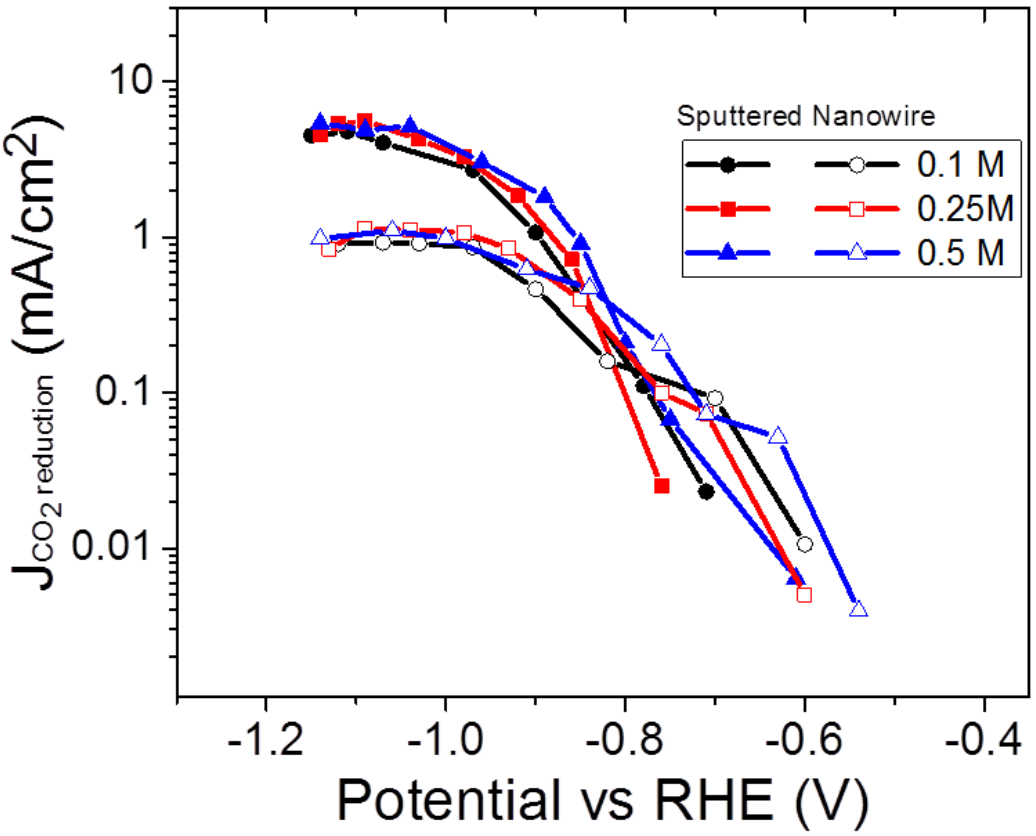

Figure S13: Electrochemically active surface area normalized partial current density for CO_2 reduction.

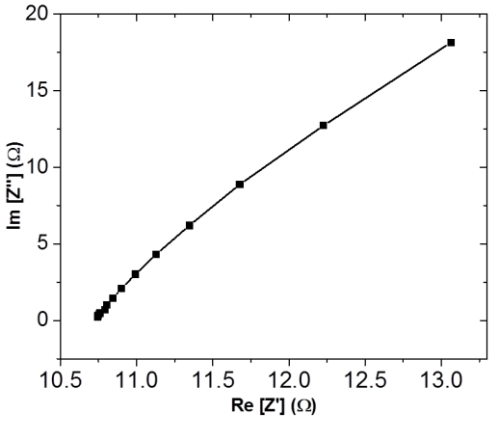

Figure S14: Electrochemical impedance spectroscopy of Cu film on Ge before SEIRAS measurements in 0.5 M phosphate buffer.

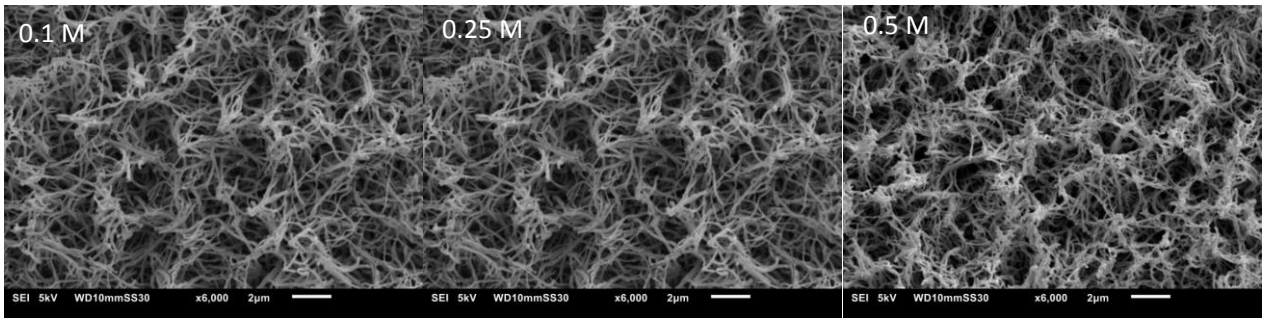

Figure S15: SEM images of the copper nanowires after electrolysis in different phosphate buffer concentrations.

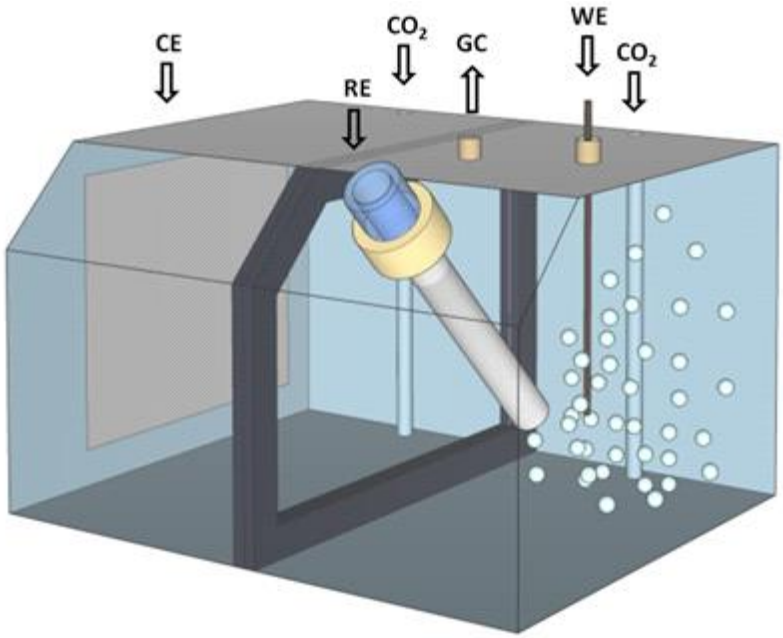

Figure S16: Illustration of the electrochemical cell used for CO2 reduction

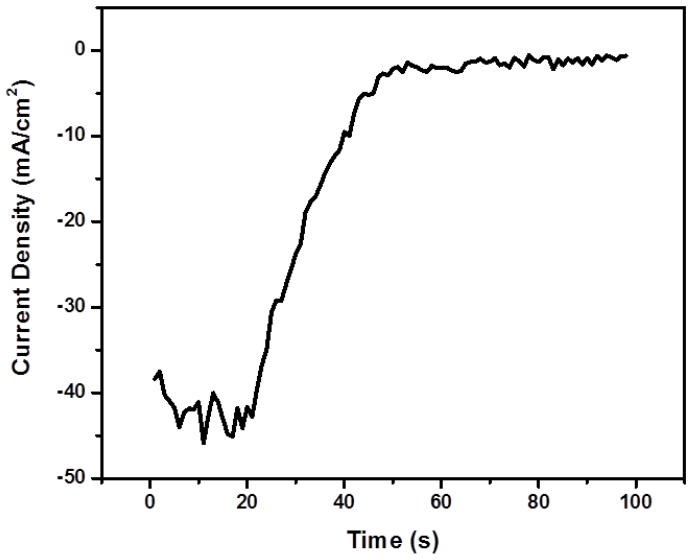

Figure S17: CuO reduction current transient at -0.8 V vs. Ag/AgCl in 0.25 M phosphate buffer.

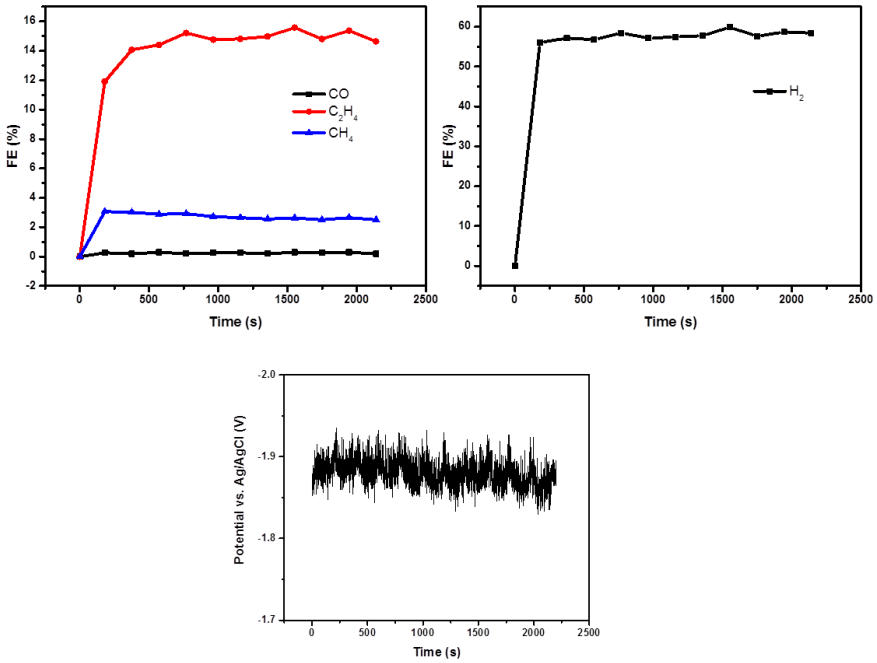

Figure S18: Change in the FE and potential as a function of time at current density of 125 mA/cm^2 in 0.5 M phosphate buffer.

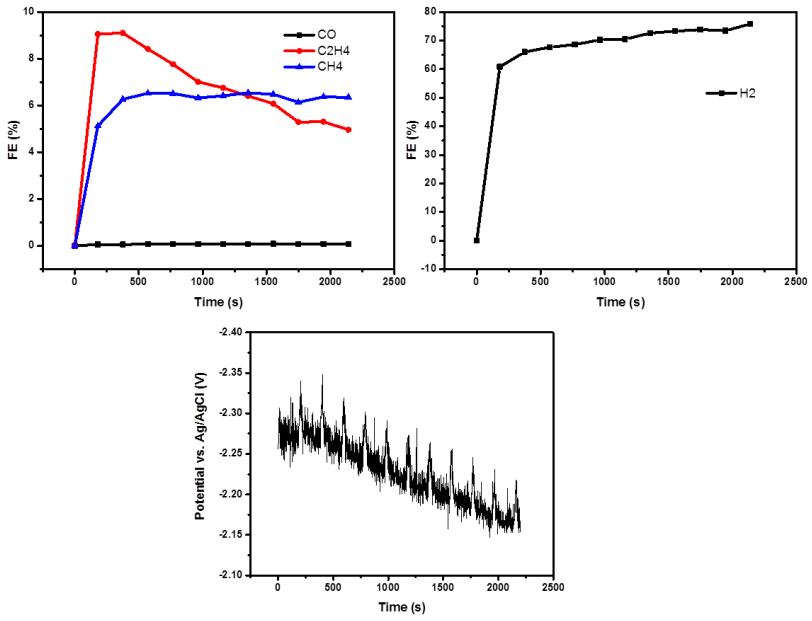

Figure S19: Change in the FE and potential as a function of time at current density of 200 mA/cm^2 in 0.5 M phosphate buffer.

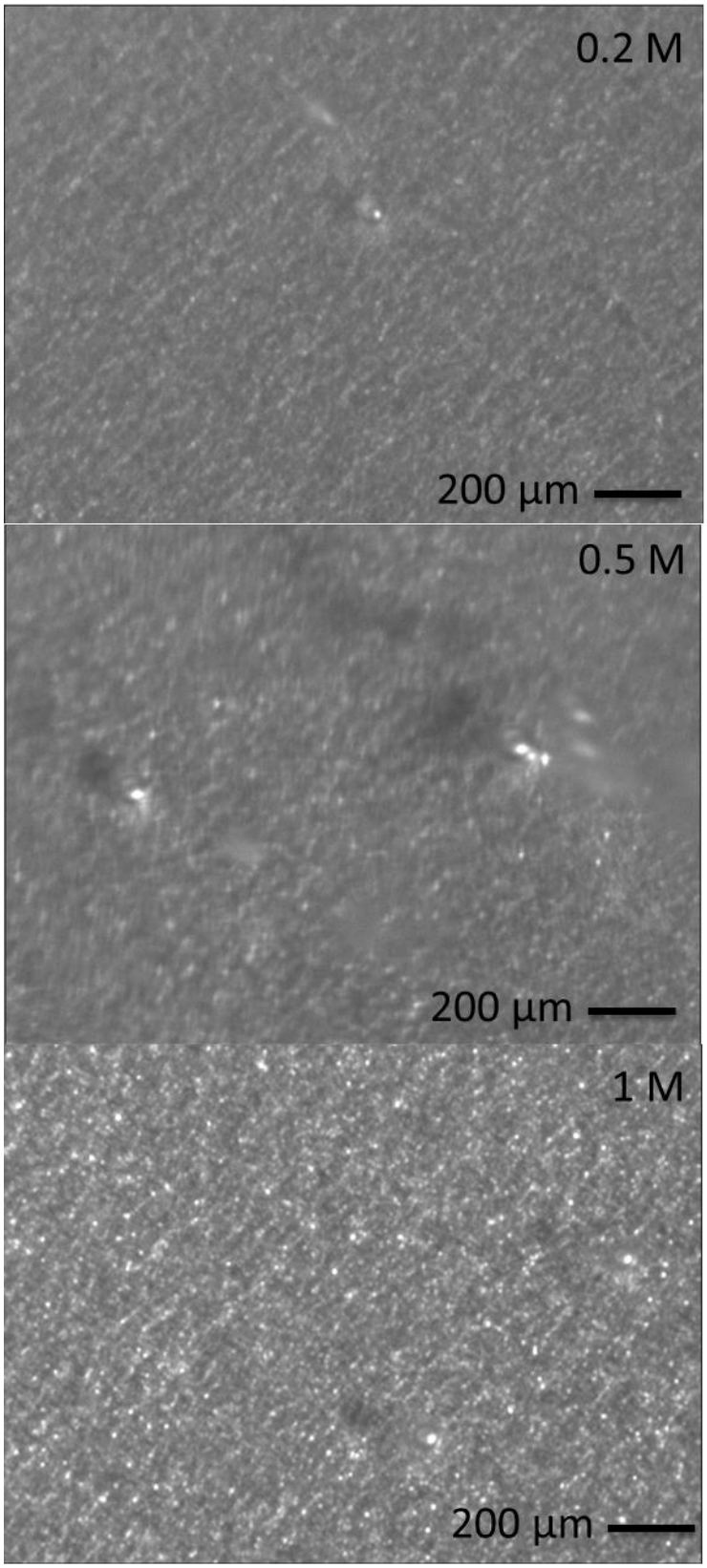

Figure S20: Bubble departure diameters as a function of electrolyte concentration were similar. The diameters were found to change between 40-70 µm in different nucleation sites as a function of current density. (25 nm thick sputtered copper films on titanium foils at 5 mA/cm^2).

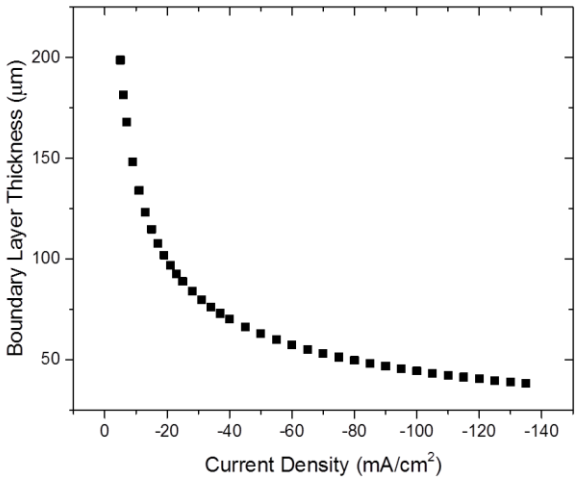

Figure S21: Effect of current density on diffusion layer thickness.

References

1. Burdyny, T.; Graham, P. J.; Pang, Y.; Dinh, C.-T.; Liu, M.; Sargent, E. H.; Sinton, D., Nanomorphology-enhanced gas-evolution intensifies CO2 reduction electrochemistry. *ACS Sustainable Chemistry & Engineering* **2017,** *5* (5), 4031-4040.
2. Gupta, N.; Gattrell, M.; MacDougall, B., Calculation for the cathode surface concentrations in the electrochemical reduction of CO 2 in KHCO 3 solutions. *Journal of applied electrochemistry* **2006,** *36* (2), 161-172.
3. Resasco, J.; Lum, Y.; Clark, E.; Zeledon, J. Z.; Bell, A. T., Effects of Anion Identity and Concentration on Electrochemical Reduction of CO2. *ChemElectroChem* **2018,** *5* (7), 1064-1072.
4. Vogt, H.; Stephan, K., Local microprocesses at gas-evolving electrodes and their influence on mass transfer. *Electrochimica Acta* **2015,** *155*, 348-356.
5. Roušar, I.; Cezner, V., Transfer of mass or heat to an electrode in the region of hydrogen evolution—I theory. *Electrochimica Acta* **1975,** *20* (4), 289-293.
6. Horsman, P.; Conway, B. E.; Yeager, E., *Comprehensive Treatise of Electrochemistry: Electrodics: Transport*. Springer US: 2013.
7. Vogt, H.; Balzer, R., The bubble coverage of gas-evolving electrodes in stagnant electrolytes. *Electrochimica Acta* **2005,** *50* (10), 2073-2079.
8. Raciti, D.; Mao, M.; Wang, C., Mass transport modelling for the electroreduction of CO2 on Cu nanowires. *Nanotechnology* **2017,** *29* (4), 044001.
9. Cohn, E. J., THE ACTIVITY COEFFICIENTS OF THE IONS IN CERTAIN PHOSPHATE SOLUTIONS A CONTRIBUTION TO THE THEORY OF BUFFER ACTION1. *Journal of the American Chemical Society* **1927,** *49* (1), 173-193.
10. Stillinger, F. H., Proton transfer reactions and kinetics in water. *Theoretical Chemistry: Advances and Perspectives, eds Eyring H, Henderson D (Academic, New York)* **1978,** *3*, 177-234.
11. Laliberté, M., Model for calculating the viscosity of aqueous solutions. *Journal of Chemical & Engineering Data* **2007,** *52* (2), 321-335.
12. Weisenberger, S.; Schumpe, d. A., Estimation of gas solubilities in salt solutions at temperatures from 273 K to 363 K. *AIChE Journal* **1996,** *42* (1), 298-300.
13. Bertheussen, E.; Verdaguer-Casadevall, A.; Ravasio, D.; Montoya, J. H.; Trimarco, D. B.; Roy, C.; Meier, S.; Wendland, J.; Nørskov, J. K.; Stephens, I. E., Acetaldehyde as an intermediate in the electroreduction of carbon monoxide to ethanol on oxide-derived copper. *Angewandte Chemie International Edition* **2016,** *55* (4), 1450-1454.
14. Ledezma-Yanez, I.; Gallent, E. P.; Koper, M. T.; Calle-Vallejo, F., Structure-sensitive electroreduction of acetaldehyde to ethanol on copper and its mechanistic implications for CO and CO2 reduction. *Catalysis Today* **2016,** *262*, 90-94.
15. Birdja, Y. Y.; Koper, M. T., The importance of cannizzaro-type reactions during electrocatalytic reduction of carbon dioxide. *Journal of the American Chemical Society* **2017,** *139* (5), 2030-2034.
16. Fan, Q.; Zhang, M.; Jia, M.; Liu, S.; Qiu, J.; Sun, Z., Electrochemical CO2 reduction to C2+ species: Heterogeneous electrocatalysts, reaction pathways, and optimization strategies. *Materials today energy* **2018,** *10*, 280-301.
17. Zhuang, T.-T.; Pang, Y.; Liang, Z.-Q.; Wang, Z.; Li, Y.; Tan, C.-S.; Li, J.; Dinh, C. T.; De Luna, P.; Hsieh, P.-L., Copper nanocavities confine intermediates for efficient electrosynthesis of C3 alcohol fuels from carbon monoxide. *Nature Catalysis* **2018,** *1* (12), 946.
18. Kuhl, K. P.; Cave, E. R.; Abram, D. N.; Jaramillo, T. F., New insights into the electrochemical reduction of carbon dioxide on metallic copper surfaces. *Energy & Environmental Science* **2012,** *5* (5), 7050-7059.
19. Gattrell, M.; Gupta, N.; Co, A., A review of the aqueous electrochemical reduction of CO2 to hydrocarbons at copper. *Journal of Electroanalytical Chemistry* **2006,** *594* (1), 1-19.

20. Li, J.; Che, F.; Pang, Y.; Zou, C.; Howe, J. Y.; Burdyny, T.; Edwards, J. P.; Wang, Y.; Li, F.; Wang, Z., Copper adparticle enabled selective electrosynthesis of n-propanol. *Nature communications* **2018,** *9* (1), 4614.
21. Calle-Vallejo, F.; Koper, M. T., Theoretical considerations on the electroreduction of CO to C2 species on Cu (100) electrodes. *Angewandte Chemie International Edition* **2013,** *52* (28), 7282-7285.
22. Ma, M.; Djanashvili, K.; Smith, W. A., Controllable hydrocarbon formation from the electrochemical reduction of CO2 over Cu nanowire arrays. *Angewandte Chemie* **2016,** *128* (23), 6792-6796.
23. Huang, Y.; Handoko, A. D.; Hirunsit, P.; Yeo, B. S., Electrochemical reduction of CO2 using copper single-crystal surfaces: effects of CO* coverage on the selective formation of ethylene. *ACS Catalysis* **2017,** *7* (3), 1749-1756.